

DOUBLE DCO⁺ RINGS REVEAL CO ICE DESORPTION IN THE OUTER DISK AROUND IM LUP

KARIN I. ÖBERG¹, KENJI FURUYA², RYAN LOOMIS¹, YURI AIKAWA³, SEAN M. ANDREWS¹,
CHUNHUA QI¹, EWINE F. VAN DISHOCK^{2,4}, AND DAVID J. WILNER¹

¹Harvard-Smithsonian Center for Astrophysics, 60 Garden St., Cambridge, MA 02138, USA

²Leiden Observatory, Leiden University, P.O. Box 9513, 2300 RA, Leiden, The Netherlands

³Center for Computational Sciences, University of Tsukuba, 1-1-1 Tennodai, Tsukuba 305-8577, Japan

⁴Max-Planck-Institut für Extraterrestrische Physik (MPE), Giessenbachstrasse 1, D-85748, Garching, Germany

Received 2015 June 29; accepted 2015 August 6; published 2015 September 4

ABSTRACT

In a protoplanetary disk, a combination of thermal and non-thermal desorption processes regulate where volatiles are liberated from icy grain mantles into the gas phase. Non-thermal desorption should result in volatile-enriched gas in disk-regions where complete freeze-out is otherwise expected. We present Atacama Large Millimeter/Submillimeter Array observations of the disk around the young star IM Lup in 1.4 mm continuum, C¹⁸O 2–1, H¹³CO⁺ 3–2 and DCO⁺ 3–2 emission at $\sim 0''.5$ resolution. The images of these dust and gas tracers are clearly resolved. The DCO⁺ line exhibits a striking pair of concentric rings of emission that peak at radii of $\sim 0''.6$ and $2''$ (~ 90 and 300 AU, respectively). Based on disk chemistry model comparison, the inner DCO⁺ ring is associated with the balance of CO freeze-out and thermal desorption due to a radial decrease in disk temperature. The outer DCO⁺ ring is explained by non-thermal desorption of CO ice in the low-column-density outer disk, repopulating the disk midplane with cold CO gas. The CO gas then reacts with abundant H₂D⁺ to form the observed DCO⁺ outer ring. These observations demonstrate that spatially resolved DCO⁺ emission can be used to trace otherwise hidden cold gas reservoirs in the outmost disk regions, opening a new window onto their chemistry and kinematics.

Key words: astrochemistry – circumstellar matter – molecular processes – protoplanetary disks – radio lines: ISM – techniques: imaging spectroscopy

1. INTRODUCTION

Planets form through the assembly of refractory dust, volatile ice, and gas in disks around young stars. The spatial distribution of volatile abundances helps determine the compositions of nascent planets that form at different disk radii. The separation of these volatiles into their gas and ice phases is set by the balance of adsorption (“freeze-out” of gas onto solids), and desorption back to the gas phase. Desorption results from both thermal and non-thermal processes that can be active in different regions of protoplanetary disks.

The thermal desorption (sublimation) rate for a volatile is set by its energy barrier for ice desorption in concert with the grain temperature. Common volatiles like H₂O, CO₂, and CO are characterized by very different desorption barriers. For a typical disk with midplane temperatures that increase closer to the host star, this range of desorption energy barriers will introduce a series of distinct locations—“snow lines”—where specific volatiles are liberated from ices into the gas phase. The highly volatile species CO and N₂ have the lowest thermal desorption barriers, and so have snow lines at large disk radii where the disk is cold, ~ 30 – 100 AU (Öberg et al. 2011a). Irradiation heating maintains a thermal inversion in the disk atmosphere, where temperatures increase with height (z) above the midplane (e.g., Calvet et al. 1991). These higher surface temperatures mean that snow lines are really two-dimensional snow surfaces whose boundaries extend to larger r for larger z .

In addition to thermal desorption, there are analogous non-thermal processes driven by interactions between ice and high-energy photons and particles, or the release of chemical energy (Garrod et al. 2007). Ice photodesorption by ultraviolet (UV) radiation has garnered special interest because of the strong UV fields produced by young stars (e.g., Bergin et al. 2003) and the high UV desorption yields measured in laboratory experiments

(Westley et al. 1995; Öberg et al. 2007; Fayolle et al. 2011; Chen et al. 2014). In the inner disk, UV photodesorption can result in lower scale heights for snow surfaces compared to the ones expected from thermal desorption (Woitke et al. 2009; Hogerheijde et al. 2011; Oka et al. 2012). At the low densities of the outer disk, UV radiation may penetrate to the cold midplane to desorb CO ice well outside the expected location of the thermal CO snowline (Willacy & Langer 2000).

DCO⁺ is expected to form efficiently in cold regions where CO gas is still present in the gas-phase, whether thermally or non-thermally desorbed, through deuteron transfer from the low-temperature ($T < 50$ K) product H₂D⁺ to CO. Therefore, the expectation is that DCO⁺ emission peaks close to the CO snow surface, i.e., at the coldest disk locations where CO is still abundant in the gas-phase if only thermal desorption is considered. Several studies have found an increasing DCO⁺ abundance with radius ascribed to this process (Qi et al. 2008; Teague et al. 2015), and Mathews et al. (2013) resolved a ring of DCO⁺ in the disk around the Herbig Ae star HD 163296, which seems closely related to the CO snow line. Their proposed connection between the DCO⁺ emission morphology and the CO snowline is challenged by new disk chemistry models, where significant DCO⁺ can be produced at temperatures above 30 K through pathways that do not involve H₂D⁺ (Favre et al. 2015). However, this complication does not eliminate the fact that DCO⁺ requires gas-phase CO to form, nor does it remove the expectation that DCO⁺ is formed in excess if H₂D⁺ is abundant (i.e., if the gas is cold).

In this study, we present Atacama Large Millimeter/Submillimeter Array (ALMA) Cycle 2 observations of the IM Lup disk, located at a distance of 155 pc (Lombardi et al. 2008), in 1.4 mm continuum, DCO⁺ 3–2, C¹⁸O 2–1 and H¹³CO⁺ 3–2 line emission (Section 2). Section 3 presents the

Table 1
Molecular Line Data

Molecular Line	Rest Freq. (GHz)	$\text{Log}_{10}(A_{ij})$	E_u (K)	Beam (PA) " × " (°)	Integrated Flux (mJy km s ⁻¹)
DCO ⁺ $J = 3-2$	216.1126	-2.62	20.7	0".65 × 0".48 (-171°)	450 ± 45
C ¹⁸ O $J = 2-1$	219.5604	-6.22	15.8	0".68 × 0".47 (-160°)	1460 ± 150
H ¹³ CO ⁺ $J = 3-2$	260.2553	-2.87	25.0	0".68 × 0".59 (89°)	484 ± 48

observed emission morphology of DCO⁺ and the other species. In Section 4 we use a disk chemistry model, applied to a generic T Tauri disk structure, to interpret the observations. We highlight the role of non-thermally desorbed CO to explain the presence of DCO⁺ emission in the outer regions of the disk in the discussion in Section 5 and summarize our findings in Section 6.

2. OBSERVATIONS AND DATA REDUCTION

Observations of the IM Lup disk were acquired with the ALMA (project code ADS/JAO.ALMA#2013.1.00226.S) on 2014 July 6 with 31 antennas (targeting DCO⁺ and C¹⁸O) and on 2014 July 17 with 32 antennas (targeting H¹³CO⁺). The antenna separations spanned baselines of 15–650 m. The total on source integration time was ~21 minutes in each execution. The nearby quasars J1534–3526 and J1427–4206 were used for gain and bandpass calibration, respectively. Titan was observed to calibrate the absolute amplitude scale.

On the July 6 execution, the correlator was configured to process 13 distinct spectral windows (SPWs). The spectral resolution $\delta\nu$ and bandwidth for 12 of the SPWs were 61 kHz and 59 MHz, respectively; the remaining SPW had a coarser resolution with a bandwidth of 469 MHz. The DCO⁺ 3–2 line was located in SPW1, and C¹⁸O 2–1 in SPW6 (Table 1). For the July 7 execution, the correlator was configured to process 14 SPWs in a different part of the Band 6 spectrum. All had the same spectral resolution, 61 kHz; 12 SPWs had a bandwidth of 59 MHz, and the remaining two had a bandwidth of 117 MHz. The H¹³CO⁺ 3–2 line (Table 1) was located in SPW1.

The visibility data were calibrated by ALMA staff. The calibration plots were inspected, deemed adequate, and no changes to the delivered calibration were made. Each individual SPW was further phase and amplitude self-calibrated in CASA 4.2.2. In each SPW, the continuum was subtracted using line-free channels. The fully calibrated visibilities were Fourier inverted and CLEANed using the Briggs weighting scheme: the robust parameter was set 0.5 for the continuum and 1.0 for the spectral lines. A CLEAN mask was manually generated based on the bright C¹⁸O 2–1 line, and then applied to the H¹³CO⁺ and DCO⁺ lines. The CLEANed maps were restored with a synthesized beam with FWHM dimensions of ~0".7 × 0".5. The 1.4 mm continuum has an rms noise level of ~0.24 mJy beam⁻¹ (dynamic range limited). The integrated flux density is 181 ± 18 mJy (which includes a 10% flux calibration uncertainty), consistent with previous SMA measurements (Öberg et al. 2011b). The resulting rms noise level in 0.2 km s⁻¹ binned channels is 4–6 mJy.

3. OBSERVATIONAL RESULTS

Figure 1 shows the continuum and integrated line emission maps of C¹⁸O 2–1, H¹³CO⁺ 3–2, and DCO⁺ 3–2 from the IM

Lup disk. The continuum is centrally peaked and spatially resolved, extending out to a radius of ~2" (300 AU), comparable to previous lower resolution observations (Pinte et al. 2008; Panić et al. 2009; Öberg et al. 2011b). The peak flux density at the disk center is 66 ± 7 mJy beam⁻¹ at 1.4 mm (C¹⁸O and DCO⁺ spectral setting) and 78 ± 8 mJy beam⁻¹ at 1.1 mm (H¹³CO⁺ spectral setting), corresponding to a brightness temperature of ~6 K.

Integrated line emission maps (Figure 1, top panel) were constructed by summing up emission from individually CLEANed 0.2 km s⁻¹-wide channels, employing a 2 σ threshold to maximize the SNR. They are shown together with the continuum 2 σ contour. The middle panel of Figure 1 presents integrated line emission maps of the same lines split up into two velocity bins around the source velocity to visualize the disk rotation. The integrated emission in these panels have been scaled to a constant emission maximum to show the increasing importance of extended emission for DCO⁺ compared to H¹³CO⁺, and for H¹³CO⁺ compared to C¹⁸O. To visualize the radial structure of these tracers more clearly and to mitigate any bias introduced by the applied clipping threshold, we also produced moment-0 maps without any clipping, deprojected and azimuthally averaged them into radial brightness profiles (Figure 1, bottom panels). We assumed an inclination of 49° and a position angle of -35° for these calculations (Pinte et al. 2008; Panić et al. 2009).

The integrated emission maps and average radial profiles reveal two significant morphological features. First, all three molecular species show a clear central depression. The C¹⁸O and DCO⁺ emission each peak at a radius of 0".6, or ~90 AU, and the H¹³CO⁺ line peaks at 0".8 (~125 AU). Second, DCO⁺ exhibits a large second ring at 2", near the outer edge of the continuum emission. No such ring is observed in C¹⁸O, H¹³CO⁺ or the continuum. However, the H¹³CO⁺ emission “plateaus” around the same radius and C¹⁸O exhibits a subtle slope change.

4. DISK CHEMISTRY MODELING

4.1. Model Description

To interpret the observed C¹⁸O, H¹³CO⁺, and DCO⁺ radial structures, we explored the relevant predictions of the disk chemistry model presented by Furuya & Aikawa (2014), Aikawa et al. (2015), updated with deuterium chemistry that considers nuclear spin (ortho/para) chemistry of light species. This model adopts a generic steady, axisymmetric Keplerian disk around a T Tauri star with stellar mass, radius, and effective temperature of $M_* = 0.5 M_\odot$, $R_* = 2 R_\odot$, and $T_* = 4000$ K, respectively, and disk mass $1.7 \times 10^{-2} M_\odot$ (Nomura et al. 2007). The stellar UV and X-ray luminosities are set to 10^{31} erg s⁻¹ and 10^{30} erg s⁻¹, respectively, based on the observed spectrum of the young star TW Hya (Herczeg

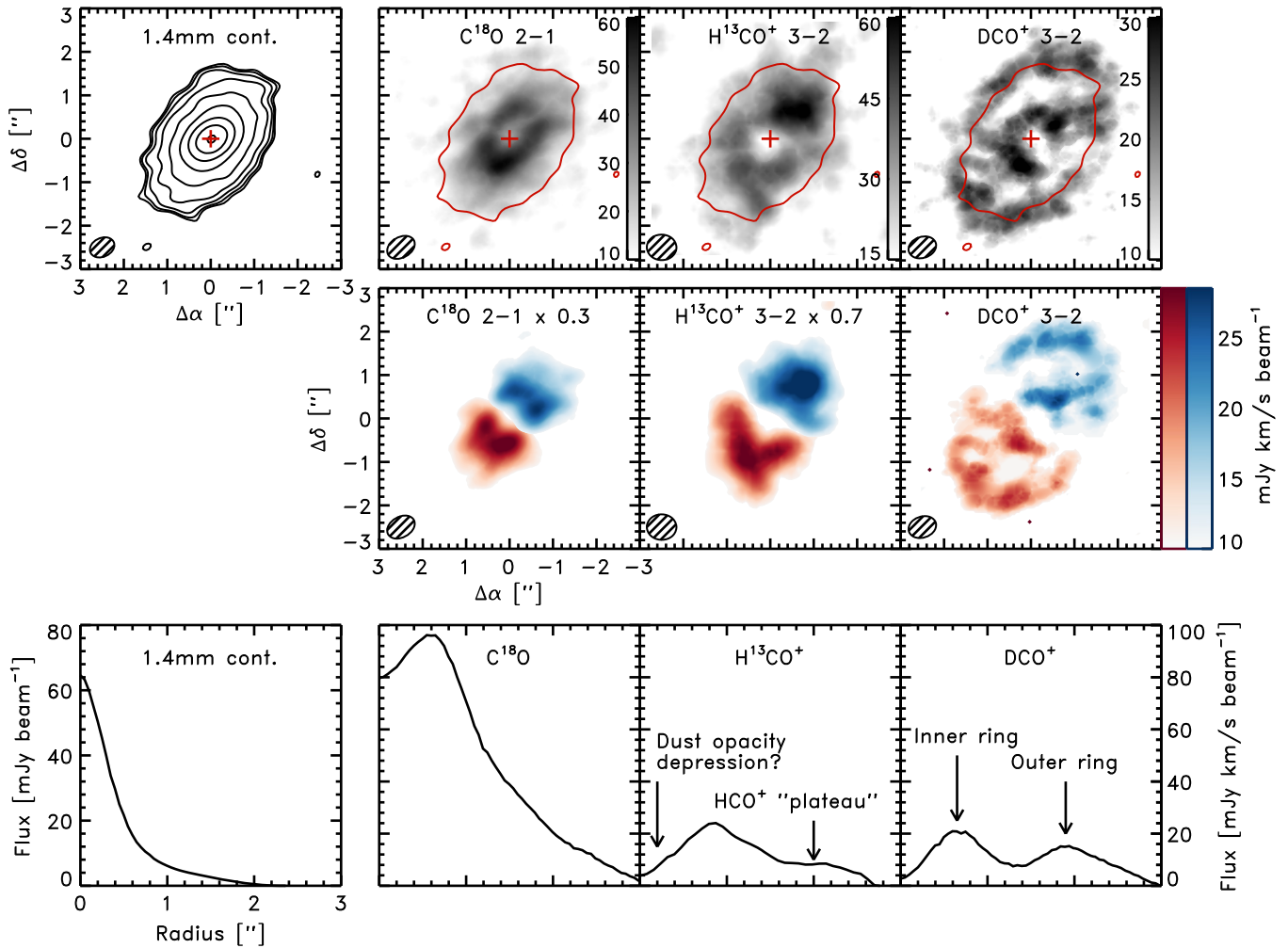


Figure 1. Continuum and integrated emission maps of C^{18}O 2–1, H^{13}CO^+ 3–2 and DCO^+ 3–2 toward IM Lup (top row), integrated emission in two velocity bins (middle row) and deprojected azimuthally averaged profiles (bottom row). Top row: the contours in the continuum map are $2\sigma + [2, 4, 8, 16, \dots]\sigma$ with the continuum rms $\sigma = 0.24$ mJy. The 2σ continuum contour is also shown on top of the integrated line emission maps. The integrated line emission in units of $\text{mJy km/s beam}^{-1}$ is shown in gray scale (see individual color bars in each panel). The continuum peak is marked by a red cross and the synthesized beam is displayed in the bottom left of each panel. Middle row: the integrated emission in two velocity bins around the source velocity has been scaled by 0.3 for C^{18}O and 0.7 for HCO^+ to enable all three line maps to be shown on the same scale (color bar to the right of the DCO^+ panel). Bottom row: the azimuthally averaged molecular emission profiles have been labeled to highlight the lack of molecular emission at the continuum maximum, and the clear DCO^+ double-ring structure.

et al. 2002; Kastner et al. 2002). The disk model assumes that the grains have grown up to 1 mm throughout the disk, resulting in a factor of 10 decrease in grain surface area compared to ISM dust. The gas temperature, dust temperature and density distributions of the disk are calculated self-consistently, considering various heating and cooling mechanisms (Nomura et al. 2007).

Compared to IM Lup, this model employs a fainter star, which results in a colder disk, and also a lower disk mass. The differences in temperature and density structure clearly precludes any quantitative comparison between the model and data. However, even though the model has not been tuned to the parameters of IM Lup, qualitative comparisons still provide valuable insight into the origins of the observed molecular emission structure, as long as the model results are robust to the model parameter choices. To evaluate the latter we performed a small parameter study where we varied the CO binding energy and the cosmic ionization rate. As described below the main results are not sensitive to these parameters. We therefore conclude that the predictions from the generic disk

model are useful for interpreting the observed emission pattern of the specific disk around IM Lup.

The chemical composition of the model is calculated by integrating a time-dependent system of gas and grain surface rate equations for 300 kyr, assuming the physical structure is static (Hasegawa et al. 1992). The gas-grain reaction network is based on the work by Garrod & Herbst (2006), supplemented with calculations that account for high-temperature gas phase reactions (Harada et al. 2010), X-ray mediated chemistry (Furuya et al. 2013, and references therein) deuterium chemistry (Aikawa et al. 2012, and references therein), and nuclear spin state chemistry of H_2 , H_3^+ and their isotopologues (Hugo et al. 2009; Coutens et al. 2014). Species containing chlorine, phosphorus, or more than four carbon atoms were excluded for computational expediency. Elemental abundances are taken from Aikawa & Herbst (2001). The initial abundances are obtained by calculating the molecular evolution of a star-forming core, following Aikawa et al. (2012).

Importantly for this study, the binding energy of CO in the generic disk model is set to 1150 K, its measured value for H_2O

ice surfaces (Collings et al. 2004), which results in a CO midplane freeze-out temperature of ~ 26 K. If CO is instead freezing out on a pure CO ice, the binding energy will be lower. We explored the effects of such a scenario by running a model with the CO binding energy set to 1000 K. Non-thermal desorption is included through stochastic heating by cosmic-rays (Hasegawa & Herbst 1993), photodesorption (Öberg et al. 2009a, 2009b; Fayolle et al. 2011; Chen et al. 2014), and reactive desorption (Garrod et al. 2007). The CO photodesorption yield is set to 7×10^{-3} (Fayolle et al. 2013). UV photodesorption and cosmic ray heating are the most important non-thermal desorption mechanisms. Their relative contributions depend on a combination of adopted yields, cosmic ray ionization rate, dust properties, and UV field, which varies across the disk.

The main target of this study, DCO^+ , forms through three different pathways in the model

1. $\text{H}_2\text{D}^+ + \text{CO} \rightarrow \text{H}_2 + \text{DCO}^+$,
2. $\text{HCO}^+ + \text{D} \rightarrow \text{DCO}^+ + \text{H}$
3. $\text{CH}_2\text{D}^+ + \text{O} \rightarrow \text{DCO}^+ + \text{H}_2$ and other pathways related to CH_2D^+ .

The D and CH_2D^+ pathways regulate DCO^+ formation at elevated temperatures, i.e., in the inner ($R < 10$ AU) disk and in the disk atmosphere at all radii. The D pathway is generally the more important of the two in the present model. Favre et al. (2015), on the other hand, argued that the CH_2D^+ path is more important, probably due to a different disk ionization structure compared to our model. Exterior to 10 AU, warm DCO^+ is a minor contribution to the total DCO^+ column density. Instead, the H_2D^+ pathway dominates the DCO^+ production. H_2D^+ forms efficiently at low temperatures due to the small (< 230 K) zero-point energy difference between H_3^+ and H_2D^+ (the exact energy difference depends on the spin states of H_2 and H_2D^+).

4.2. Model Results and Comparison to Observations

Figure 2 shows the model disk temperature and density structure. One particular difference worth highlighting between this generic model and IM Lup is in the disk midplane temperature profile. In the model, 20 K is reached at a radius of ~ 40 AU, while a previous analysis of the IM Lup disk suggests that 20 K is reached at a larger radius (~ 40 –100 AU), dependent in detail on the model assumptions (Pinte et al. 2008).⁵ As a result, CO freeze-out in this model probably starts at smaller radii compared to the IM Lup disk.

These model calculations do not include C and O isotope-specific chemistry. To make comparisons with the observations of isotopologues we have scaled the calculated CO and HCO^+ abundances by factors of 500 and 70, respectively, adopting the standard ISM $^{16}\text{O}/^{18}\text{O}$ and $^{12}\text{C}/^{13}\text{C}$, to estimate the C^{18}O and H^{13}CO^+ abundances. We expect that this is a reasonable approximation in the disk midplane (in the disk atmosphere, isotopologue specific photodissociation rates will change the relative CO isotopologue abundances Miotello et al. 2014).

Figure 2 (middle row) shows the radial and vertical gas-phase abundance profiles for the species that are the focus of this study, i.e., CO, HCO^+ and DCO^+ , with the first two abundances scaled to correspond to the observed isotopologues. All three molecules exhibit an abundance depression in the disk midplane exterior to 25 AU due to freeze-out of CO

onto grain surfaces (i.e., the midplane CO snow line). Between 25 and 50 AU, the CO abundance decreases by seven orders of magnitude, the HCO^+ and DCO^+ abundance by five orders of magnitude.

Exterior to 90 AU, the CO, HCO^+ and DCO^+ gas-phase midplane abundances begin to increase. With decreasing density, the freeze-out rate decreases, which changes the CO desorption/freeze-out balance and therefore increases the gas/solid ratio. The accompanying decrease in column density results in increased UV penetration and therefore CO ice UV photodesorption, further increasing the CO gas/solid ratio. The result is a substantial amount of CO gas in the cold, outer disk midplane, corresponding to a C^{18}O abundance of $\sim 10^{-11}$ with respect to n_{H} . This is six orders of magnitude above the abundance minimum found at 50 AU, but still small compared to the total C^{18}O abundance of $\sim 10^{-7}$, i.e., most CO (isotopologues) are present in the form of ice in the outer disk midplane. By contrast, a C^{18}O abundance of $\sim 10^{-7}$ is reached in the warm molecular disk layer, $Z/R \sim 0.3$ –0.5, and this is the main reservoir of C^{18}O gas in the outer disk.

HCO^+ and DCO^+ are also present in the warm molecular disk layer, but this layer is no longer the dominant reservoir. In the case of DCO^+ , the midplane and molecular layer abundances are comparable. The relatively high DCO^+ abundance in the midplane, at $Z/R < 0.2$, is due to the increased efficiency of DCO^+ production at low temperatures. Because of an increasing gas density toward the disk midplane, the vertically integrated DCO^+ column density is dominated by the midplane DCO^+ in the outer disk. HCO^+ presents intermediate trends between CO and DCO^+ .

We calculated disk emission spectral data cubes using the 3D Monte Carlo radiative transfer code LIME (Brinch & Hogerheijde 2010) from the model disk density, temperature and molecular abundance structures, for the observed C^{18}O , H^{13}CO^+ and DCO^+ lines. Figure 2 (bottom row) shows the radial emission profiles (arbitrary units) of the C^{18}O , H^{13}CO^+ and DCO^+ obtained from the model spectral-image data cubes, integrated in velocity space and azimuthally averaged like the data. The C^{18}O emission profile is centrally peaked. It shows a radial gradient small change at ~ 25 AU at the onset of CO freeze-out. The effect of CO gas in the midplane beyond 90 AU on the CO emission profile is subtle, and in practice unobservable, since the overall column density and thus emission at these radii is dominated by the abundant gas-phase CO in the warmer atmosphere layers.

The HCO^+ and DCO^+ emission profiles decrease rapidly at radii of 25–40 AU, due to the freeze-out of gas-phase CO (their formation reservoir). The HCO^+ emission then presents a “plateau” out to 100 AU, attributed to Cosmic Ray and UV photodesorption of CO back into the gas phase. The effect of the midplane CO non-thermal desorption on the DCO^+ emission is, as expected, more dramatic. The return of CO to the gas at large radii, where low temperatures drives an efficient deuterium fractionation chemistry, results in a second maximum (outer ring) peaking at 200 AU. DCO^+ also presents a small peak toward the central star, caused by warm deuterium fractionation chemistry, and an inner ring close to the CO midplane snow line. Unlike for CO emission, the presence of cold CO in the outer midplane has a considerable effect on HCO^+ and DCO^+ emission, which should be observable.

Based on a small grid of models the shapes of the predicted CO, HCO^+ and DCO^+ radial profiles are not sensitive to

⁵ We have corrected for the assumed distance of 190 pc.

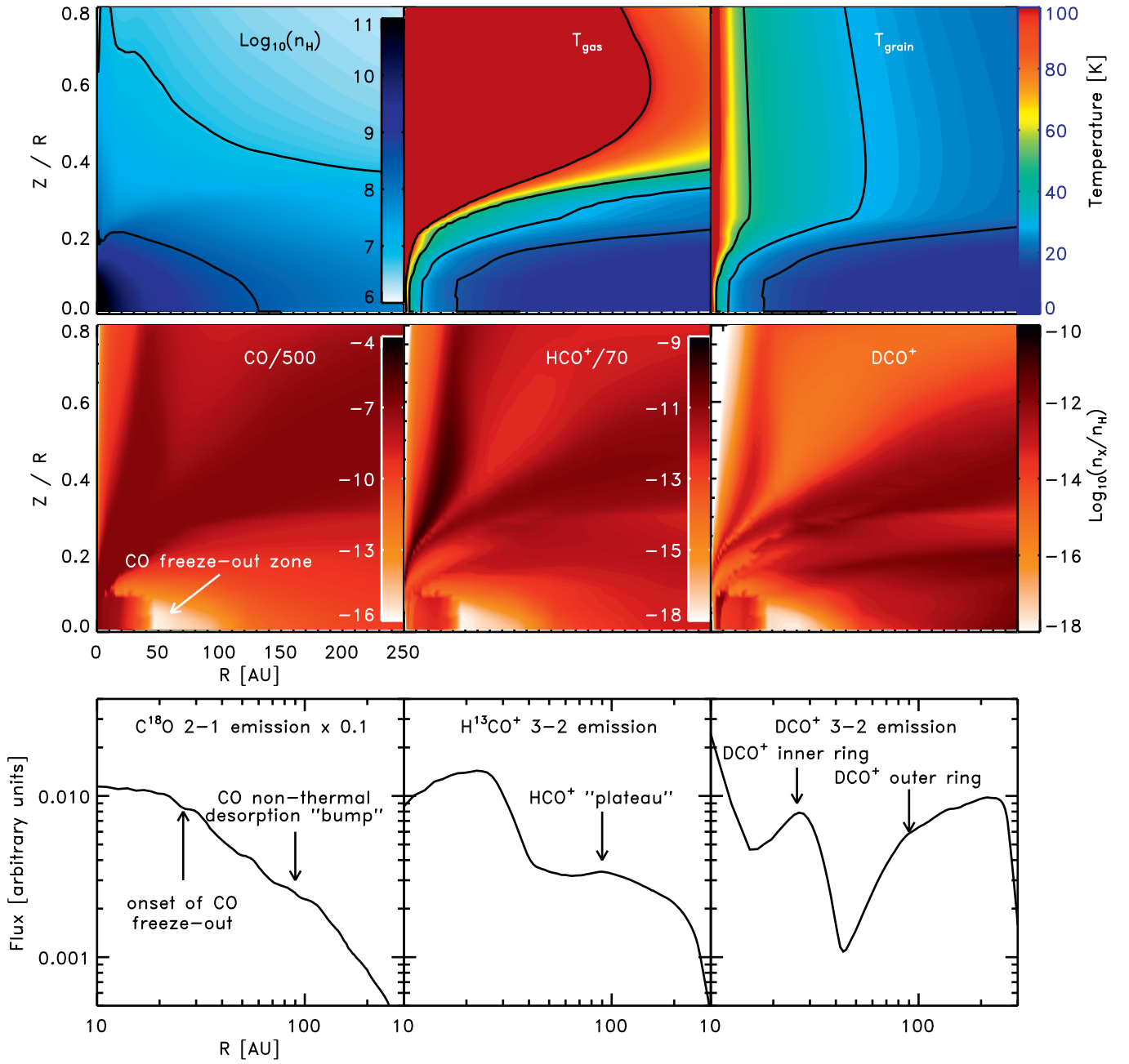


Figure 2. Density, gas and dust grain temperatures in our generic disk model (top row) and the $\text{CO}/500$ ($\sim\text{C}^{18}\text{O}$), $\text{HCO}^+/70$ ($\sim\text{H}^{13}\text{CO}^+$) and DCO^+ abundances with respect to H nuclei after 300 kyr (middle row). The density contours mark $n_{\text{H}} = 10^7$ and 10^9 cm^{-3} (upper left panel). The temperature contours mark 20, 30, 50 and 100 K (upper middle and right panels). The bottom row shows the calculated radial emission profiles of the observed lines C^{18}O 2-1, H^{13}CO^+ 3-2 and DCO^+ 3-2.

specific model assumptions. In particular the two concentric DCO^+ rings are reproduced when changing the CO binding energy from 1150 to 1000 K, i.e., from a water to a CO dominated ice environment, and when the CR ionization rate is reduced to 10^{-20} s^{-1} . In the latter case UV photodesorption still maintains cold CO gas in the outer disk, albeit at a lower level compared to when a high cosmic ray ionization rate is assumed. That is, the outer ring is still present when the cosmic ray ionization is attenuated, but it may be less pronounced. The molecular emission trends in Figure 2 thus appears to be robust as long as some non-thermal desorption process is active in the disk midplane. However, the absolute DCO^+ column density and predicted emission profile in the

outer disk do depend on model parameters, and whether the predicted DCO^+ double-ring will be observable may thus vary from disk to disk.

Qualitatively, the observed and predicted CO, HCO^+ and DCO^+ radial profiles agree well. In particular, the model reproduces several key features of the IM Lup observations: the centrally peaked C^{18}O emission profile, the H^{13}CO^+ shoulder in the outer disk, and the DCO^+ inner ring and outer ring. However, the model shows no signs of a central depression for C^{18}O , and only a very small depression for H^{13}CO^+ . For DCO^+ , the model double-ring is accompanied by an emission peak at the disk center, which is also not observed.

5. DISCUSSION

5.1. The DCO⁺ Outer Disk Ring

The most surprising result from the ALMA observations is the clear detection of a concentric pair of emission rings in the DCO⁺ 3–2 spectral line, peaking at radii of ~ 90 and 300 AU. Based on the midplane temperature profile for the IM Lup disk that was inferred from previous measurements (Pinte et al. 2008; Panić et al. 2009), the inner ring may coincide with the onset of CO freeze-out. The relationship between the CO midplane snowline and the inner DCO⁺ ring location is, however, complicated by multiple DCO⁺ formation pathways in the inner disk.

The outer DCO⁺ ring requires the return of some CO into the gas-phase at large disk radii. This can be accomplished by either non-thermal ice desorption or a radial thermal inversion in the low density outer region. Of the two scenarios we favor the former, since it naturally explains the large DCO⁺ enhancement and the much smaller H¹³CO⁺ enhancement at large disk radii. This could be observationally checked by observing additional DCO⁺ and H¹³CO⁺ lines that constrain the gas temperature.

The location of the outer DCO⁺ ring coincides with the disappearance of mm-grain emission (Figure 1). It may also coincide with a steepening of the gas-density profile (Panić et al. 2009). The radial profile of smaller grains, which carry most of the opacity at UV wavelengths, is not known independently, but it seems reasonable to assume that it too is steepening at the same radius. The DCO⁺ outer ring then likely coincides with a disk location where the UV radiation penetration depth is increasing rapidly with radius. The connection between the DCO⁺ outer ring and UV radiation is supported by chemical modeling. An outer DCO⁺ ring is produced when CO is non-thermally desorbed from icy grains in the cold, low-density outer disk. In the model UV photodesorption and CR heating are both important, but the coincidence between the ring and the loss of dust opacity suggests that in the case of IM Lup, UV photodesorption is the most important desorption mechanism in the outer disk. Once in the gas phase, CO can be chemically converted into DCO⁺ following deuterium transfers from abundant reservoirs of H₂D⁺ and other deuterated H₃⁺ isotopologues (which are enhanced at such low temperatures). This effect is expected to be generally present in disks and especially pronounced in disks with significant grain growth, which reduces UV opacity. In our model we assume a uniform grain growth throughout the disk, parameterized as a reduction in total grain surface area by a factor of 10. Further grain growth is likely present in older disks, and it may therefore be illustrative to compare the DCO⁺ distribution in disks of different ages and with different grain properties as estimated from continuum observations (Pérez et al. 2012; Andrews et al. 2014).

Based on the discussion above and the seemingly robust model results in Section 4.2, it is tempting to conclude that concentric DCO⁺ rings should be commonly observed in protoplanetary disks. It is important to realize however, that the expected intensity of the second DCO⁺ ring is model dependent. Teague et al. (2015), for example, finds a DCO⁺ enhancement in the outer disk, but it is small compared to the findings in our model. The same is true in the model by Willacy (2007). In general, the DCO⁺ abundance in the outer disk will depend on the intensity and penetration depths of radiation

fields (UV, cosmic rays and X-rays), and the DCO⁺ ring column density will depend on the total amount of cold molecular gas exposed to this radiation. The intensity of the DCO⁺ ring will also depend on the excitation conditions that characterize the outer disk midplane, especially its density and temperature. It may very well be that DCO⁺ rings, while common, are only observable in a small sub-set of disks where disk density, temperature and radiation structures conspire to produce sufficient amounts of DCO⁺ flux at large disk radii. Still the detection of one such outer ring in the IM Lup disk demonstrates that non-thermal desorption in general, and UV photodesorption of CO in particular, is important in setting the chemical structure of protoplanetary disks.

5.2. Origins of the Central Depression in Several Tracers

A lingering puzzle in the observations presented here is the central depression in the intensities of all the observed spectral lines (but notably not in the continuum). We consider four potential explanations for these depressions: (1) a reduction in the gas surface densities; (2) line of sight absorption by foreground cloud material; (3) unexpected chemistry; and (4) high continuum optical depths that prevent some of the line emission from escaping the disk.

The first possibility seems unlikely, since there is no analogous signature in the continuum, and we are unaware of a physical mechanism that would systematically enhance the mm dust-to-gas ratio in the inner disk. The second scenario, molecular cloud contamination, should produce deeper depressions (absorption) for the more optically thick spectral lines. Inspection of CO data toward the same source show that CO exhibits less visible depressions than C¹⁸O, ruling out this scenario.

Chemistry can produce central depressions in HCO⁺ and DCO⁺ following desorption of H₂O and other molecules with high proton affinity in the inner disk, resulting in efficient proton transfer from HCO⁺ and DCO⁺ to H₂O. Chemistry may thus contribute to the H¹³CO⁺ and DCO⁺ holes. The C¹⁸O central depression is not predicted by our or any other published disk chemistry model (e.g., Willacy & Woods 2009; Walsh et al. 2010; Semenov & Wiebe 2011), though the conversion efficiency of CO into other species across the disk is an active topic of research (e.g., Favre et al. 2013). Based on the results presented so far, it seems unlikely, however, that chemistry alone can explain the entire observed effect.

The last proposed explanation is that the continuum optical depths in the disk center are high enough to block some of the line emission from the midplane. The deeper depressions observed for more optically thin tracers, which originate closer to the midplane, and for lines emitted at higher frequencies (especially H¹³CO⁺) supports this scenario. But this scenario has one significant problem: the peak continuum intensity at the disk center corresponds to a brightness temperature of only 6 K, much lower than expected for optically thick emission at these radii. The only way of reconciling this explanation with the data is through significant beam dilution. If the optically thick continuum emission is concentrated in small scale features (occupying an area $\sim 5\times$ smaller than the synthesized beam), then this scenario may work. That may seem unlikely, but the recent observations of the HL Tau disk showing small scale structure (ALMA Partnership et al. 2015) indicate that it remains a possibility. This hypothesis could be tested directly by very high spatial resolution continuum measurements, or

less directly by observations of CO and HCO⁺ isotopologue lines at 3 mm, where the dust opacity should be reduced.

6. SUMMARY AND CONCLUSIONS

ALMA observations of the massive disk around IM Lup have revealed a spectacular DCO⁺ double-ringed structure. The inner ring appears connected with the thermal CO snowline, but dust opacity and multiple DCO⁺ formation pathways complicate the interpretation. The second, outer DCO⁺ emission ring at 300 AU is readily reproduced by non-thermal CO ice desorption in the low-density, outer disk. The ring coincides with a rapid decrease in dust opacity, which is likely accompanied by increased UV penetration toward the disk midplane. We hypothesize that the DCO⁺ outer ring is caused by efficient UV photodesorption of CO ice at this radius.

Without the presence of non-thermal desorption this outer disk region would be completely devoid of CO gas and thus of CO-gas-mediated chemistry. Even at its most efficient, non-thermal desorption in disk mid planes is not expected to maintain a large fraction of CO in the gas-phase, <0.1% of the total CO reservoir. The presented observations and models show, however, that the release of such trace amounts of CO into the gas-phase can still produce an observable signature through its effects on DCO⁺ production. This DCO⁺ can be used as a probe of the kinematics and ionization in the outer disk midplane, opening up a new window on the structures of protoplanetary disks.

We are grateful to Ugo Hincelin and Eric Herbst for providing rates and branching ratios for ortho/para chemistry. This paper makes use of the following ALMA data: ADS/JAO.ALMA#2013.1.00226.S. ALMA is a partnership of ESO (representing its member states), NSF (USA) and NINS (Japan), together with NRC (Canada) and NSC and ASIAA (Taiwan), in cooperation with the Republic of Chile. The Joint ALMA Observatory is operated by ESO, AUI/NRAO and NAOJ. The National Radio Astronomy Observatory is a facility of the National Science Foundation operated under cooperative agreement by Associated Universities, Inc. K.I.Ö. also acknowledges funding from the Alfred P. Sloan Foundation, and the Packard Foundation. K.F. is supported by a Research Fellowship from the Japan Society for the Promotion of Science (JSPS). Astrochemistry in Leiden is by A-ERC grant 291141 CHEMPLAN and a KNAW professorship prize.

Facility: ALMA.

REFERENCES

- Aikawa, Y., Furuya, K., Nomura, H., & Qi, C. 2015, *ApJ*, 807, 120
Aikawa, Y., & Herbst, E. 2001, *A&A*, 371, 1107
Aikawa, Y., Wakelam, V., Hersant, F., Garrod, R. T., & Herbst, E. 2012, *ApJ*, 760, 40
ALMA Partnership, Brogan, C. L., Perez, L. M., et al. 2015, *ApJL*, 808, L3
Andrews, S. M., Chandler, C. J., Isella, A., et al. 2014, *ApJL*, 787, 148
Bergin, E., Calvet, N., D'Alessio, P., & Herczeg, G. J. 2003, *ApJL*, 591, L159
Brinch, C., & Hogerheijde, M. R. 2010, *A&A*, 523, A25
Calvet, N., Patino, A., Magris, G. C., & D'Alessio, P. 1991, *ApJ*, 380, 617
Chen, Y.-J., Chuang, K.-J., Muñoz Caro, G. M., et al. 2014, *ApJ*, 781, 15
Collings, M. P., Anderson, M. A., Chen, R., et al. 2004, *MNRAS*, 354, 1133
Coutens, A., Jørgensen, J. K., Persson, M. V., et al. 2014, *ApJL*, 792, L5
Favre, C., Bergin, E. A., Cleeves, L. I., et al. 2015, *ApJ*, 808, 155
Favre, C., Cleeves, L. I., Bergin, E. A., Qi, C., & Blake, G. A. 2013, *ApJL*, 776, L38
Fayolle, E. C., Bertin, M., Romanzin, C., et al. 2011, *ApJL*, 739, L36
Fayolle, E. C., Bertin, M., Romanzin, C., et al. 2013, *A&A*, 556, A122
Furuya, K., & Aikawa, Y. 2014, *ApJ*, 790, 97
Furuya, K., Aikawa, Y., Nomura, H., Hersant, F., & Wakelam, V. 2013, *ApJ*, 779, 11
Garrod, R. T., & Herbst, E. 2006, *A&A*, 457, 927
Garrod, R. T., Wakelam, V., & Herbst, E. 2007, *A&A*, 467, 1103
Harada, N., Herbst, E., & Wakelam, V. 2010, *ApJ*, 721, 1570
Hasegawa, T. I., & Herbst, E. 1993, *MNRAS*, 263, 589
Hasegawa, T. I., Herbst, E., & Leung, C. M. 1992, *ApJS*, 82, 167
Herczeg, G. J., Linsky, J. L., Valenti, J. A., Johns-Krull, C. M., & Wood, B. E. 2002, *ApJ*, 572, 310
Hogerheijde, M. R., Bergin, E. A., Brinch, C., et al. 2011, *Sci*, 334, 338
Hugo, E., Asvany, O., & Schlemmer, S. 2009, *JChPh*, 130, 4302
Kastner, J. H., Huenemoerder, D. P., Schulz, N. S., Canizares, C. R., & Weintraub, D. A. 2002, *ApJ*, 567, 434
Lombardi, M., Lada, C. J., & Alves, J. 2008, *A&A*, 489, 143
Mathews, G. S., Klaassen, P. D., Juhász, A., et al. 2013, *A&A*, 557, A132
Miotello, A., Bruderer, S., & van Dishoeck, E. F. 2014, *A&A*, 572, A96
Nomura, H., Aikawa, Y., Tsujimoto, M., Nakagawa, Y., & Millar, T. J. 2007, *ApJ*, 661, 334
Öberg, K. I., Bottinelli, S., & van Dishoeck, E. F. 2009a, *A&A*, 494, L13
Öberg, K. I., Fuchs, G. W., Awad, Z., et al. 2007, *ApJL*, 662, L23
Öberg, K. I., Murray-Clay, R., & Bergin, E. A. 2011a, *ApJL*, 743, L16
Öberg, K. I., Qi, C., Fogel, J. K. J., et al. 2011b, *ApJ*, 734, 98
Öberg, K. I., van Dishoeck, E. F., & Linnartz, H. 2009b, *A&A*, 496, 281
Oka, A., Inoue, A. K., Nakamoto, T., & Honda, M. 2012, *ApJ*, 747, 138
Panić, O., Hogerheijde, M. R., Wilner, D., & Qi, C. 2009, *A&A*, 501, 269
Pérez, L. M., Carpenter, J. M., Chandler, C. J., et al. 2012, *ApJL*, 760, L17
Pinte, C., Padgett, D. L., Ménard, F., et al. 2008, *A&A*, 489, 633
Qi, C., Wilner, D. J., Aikawa, Y., Blake, G. A., & Hogerheijde, M. R. 2008, *ApJ*, 681, 1396
Semenov, D., & Wiebe, D. 2011, *ApJS*, 196, 25
Teague, R., Semenov, D., Guilloteau, S., et al. 2015, *A&A*, 574, A137
Walsh, C., Millar, T. J., & Nomura, H. 2010, *ApJ*, 722, 1607
Westley, M. S., Baragiola, R. A., Johnson, R. E., & Baratta, G. A. 1995, *Natur*, 373, 405
Willacy, K. 2007, *ApJ*, 660, 441
Willacy, K., & Langer, W. D. 2000, *ApJ*, 544, 903
Willacy, K., & Woods, P. M. 2009, *ApJ*, 703, 479
Woitke, P., Kamp, I., & Thi, W.-F. 2009, *A&A*, 501, 383